Research Article | Vol. 29, No. 20 / 27 Sep 2021 / Optics Express 32365

Optics EXPRESS

Metal-insulator-metal waveguide-based optical pressure sensor embedded with arrays of silver nanorods

INFITER TATHFIF,* AHMAD AZUAD YASEER, KAZI SHARMEEN RASHID, AND RAKIBUL HASAN SAGOR

Department of Electrical and Electronic Engineering, Islamic University of Technology, Gazipur- 1704, Bangladesh
infitertathfif@iut-dhaka.edu

Abstract: An optical Metal-Insulator-Metal (MIM) pressure sensor loaded with arrays of silver nanorods (NRs) is proposed in this article. The illustrated sensor contains a straight waveguide coupled with a ladder-shaped resonator. The spectral profile of the proposed schematic is numerically analyzed utilizing the 2D Finite Element Method (FEM). When pressure is exerted upon the silver layer, the resonating area deforms and shifts the resonant wavelength. Extensive computations demonstrate that increasing the deformation shifts the resonant wavelength to the right, establishing a linear relationship. The suggested structure reports maximum pressure sensitivity of 25.4 nm/MPa. Moreover, the impact of NRs on pressure sensitivity is extensively investigated and the results indicate that the designed layout is sensitive to the size and radius of NRs, making it highly tunable. All these features make the modeled prototype a promising nanoscale solution in different fields of engineering.

1. Introduction

The ability of plasmonic structures to confine light into an enhanced subwavelength scale has provided myriads of fundamental insights into nanophotonic research endeavors. Researchers are now exploring new regimes of nano-metallic structures to analyze the light-matter interaction, and the theory of Surface Plasmon Polaritons (SPPs) helps elucidate this synergy. SPPs are electromagnetic (EM) waves propagating along the metal-dielectric juncture due to collective oscillations of electrons and photons at the resonant frequency [1–5]. The waves bind firmly at the metal surface, acquiring a unique capability to overcome the diffraction limit of light [6–9]. These properties of SPPs have pervaded a wide area of study, including sensors [10–13], absorbers [14–16], filters [17], splitters [18], photonic integrated circuits [19], and switches [20].

An SPP-based pressure sensor is an optical device that intercepts applied pressure and translates it into optical signals. Optical pressure sensors have the advantage of being impervious to electromagnetic interference, have high sensitivity, signal transmission flexibility, and inexpensive manufacturing costs [21,22]. In recent times, optical pressure sensing devices have been designed in a variety of ways to facilitate different lab-on-a-chip activities. Osorio *et al.* [23] illustrated a photonic-crystal fiber (PCF) pressure sensor for dual environment monitoring. A hybrid dual-core PCF was employed as a hydrostatic pressure sensor with a sensitivity of 0.0116 nm/MPa [24]. A nano-pressure sensor utilizing a high-quality photonic crystal cavity resonator exhibited maximum sensitivity of 0.0117 nm/MPa [25]. Another highly sensitive optical fiber pressure sensor based on a thin-walled oval cylinder stated a sensitivity of 1.198 nm/MPa [26]. Zhao *et al.* [27] suggested a nano-optomechanical pressure sensor based on a ring resonator with a sensitivity of 1.47 nm/MPa. The sensitivity of a polarization-maintaining PCF was 3.42 nm/RIU [28]. Yao *et al.* [29] developed a fiber-tip pressure sensor with a maximum sensitivity of 4.29 nm/MPa.

#439974 https://doi.org/10.1364/OE.439974
Journal © 2021 Received 6 Aug 2021; revised 9 Sep 2021; accepted 10 Sep 2021; published 23 Sep 2021

Optics EXPRESS

The MIM waveguide is one of the most prevalent SPP waveguides due to its long propagation length, strong field confinement at the subwavelength scale, and fabrication ease [30–32]. Therefore, distinctive designs of optical pressure sensors utilizing MIM waveguide are also investigated. For example, Wu *et al.* [33] reported a MIM H-shaped resonator with a sensitivity of 2.12 nm/MPa. The maximum sensitivity of a MIM pressure sensor made up of concentric square disk and ring resonators was 5 nm/MPa [4]. A π-shaped resonator based on MIM geometry demonstrated a sensitivity of 8.5 nm/MPa [34]. Palizvan *et al.* [35] proposed an optical MIM pressure sensor based on a double square ring resonator with a sensitivity of 16.5 nm/MPa. However, the pressure sensors mentioned above lack the high sensitivity needed for diverse mechanical, electrical, and biomedical applications [36].

An ultra-compact optical pressure sensor based on MIM geometry is presented in this article. The proposed structure encompasses a straight waveguide and a ladder-shaped resonator, loaded with silver NRs. The transmittance spectrum of the proposed sensor is analyzed numerically and the relation between deformation and wavelength shift is determined when pressure is applied. The suggested layout exhibits maximum pressure sensitivity of 25.4 nm/MPa. To the best of the authors' knowledge, this is the first-ever study of a pressure sensor utilizing NRs, and the sensitivity demonstrated is the highest to date in the literature.

2. Setup and MIM theory

The two-dimensional (2D) schematic representation of the proposed structure is shown in Fig. 1, where the white and grey regions represent air and silver, respectively. The 2D domain is chosen for structure modeling for efficient and fast computation [37]. The suggested sensor consists of a straight waveguide coupled with a ladder-shaped resonator. The resonator contains two horizontal slots and two vertical slots. Moreover, the waveguide and the lower horizontal slot are loaded with silver NRs. The initial structure parameters labeled in Fig. 1 are listed in Table 1.

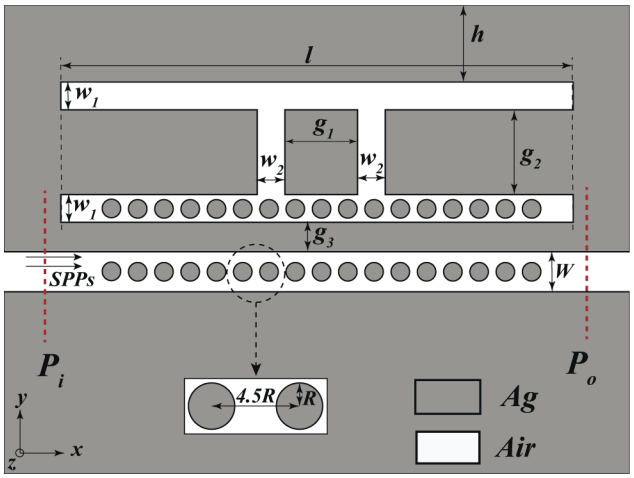

Fig. 1. Two-dimensional setup of the modeled pressure sensor.

To cover the range of the resonant wavelength, a polychromatic light source, such as a halogen lamp, can be used in the practical setup. The light reaches the input side of the pressure sensor through a single-mode fiber (SMF) [38]. The elastic membranes of a diaphragm are attached to the silver layer where the pressure will be exerted (Fig. 2(a)). Injecting fluid or gas into the diaphragm displaces its arms, generates pressure, and deforms the resonator by d nm (Fig. 2(b)) [39]. The output side of the pressure sensor is connected to an optical spectrum analyzer (OSA)

Optics EXPRESS

Table 1. Initial structural parameters.

Parameter	Symbol	Value
Waveguide width	W	50 nm
Thickness of top silver layer	h	100 nm
Horizontal slot length	l	800 nm
Horizontal slot width	w_1	40 nm
Vertical slot width	w_2	40 nm
Gap between two vertical slots	g_1	100 nm
Gap between two horizontal slots	g_2	100 nm
Gap between waveguide and lower horizontal slot	g_3	10 nm
Radius of silver NRs	R	10 nm
Number of silver NRs in waveguide	n_1	17
Number of silver NRs in lower horizontal slot	n_2	17
Period of silver NRs	-	$4.5R$ = 45 nm

through another SMF to track the changes in resonant wavelength due to the deformation. During the simulation, the width of upper horizontal slot is decreased from 40 nm to 30 nm to emulate deformation of 0 nm to 10 nm. Furthermore, W is set to 50 nm to ensure the propagation of fundamental transverse-magnetic (TM_0) mode [40]. The dispersion relation of a MIM waveguide can be characterized through the following equation [41],

$$\tanh\left(k_1 W/2\right) = -\varepsilon_{air} k_2 / \varepsilon_{silver} k_1, \tag{1}$$

where, W denotes the width of the waveguide, and the wave vectors k_1 and k_2 are defined by momentum conservations as [33],

$$\begin{aligned} k_1 &= \sqrt{\beta^2 - \mu_{air}\varepsilon_{air}k_0^2}, \\ k_2 &= \sqrt{\beta^2 - \mu_{silver}\varepsilon_{silver}k_0^2}, \end{aligned} \tag{2}$$

where, $\beta = n_{eff} \times k_0$ denotes the propagation constant of the MIM waveguide (n_{eff} = effective refractive index). k_0 refer to the free-space wave vector which can be defined as,

$$k_0 = \frac{2\pi}{\lambda} = \frac{\omega}{c}, \tag{3}$$

where, λ is the wavelength of the light, ω is the angular frequency, and c is the light speed in free space. Using Eq. (1) and Eq. (2), the resulting dispersion plot for the modeled sensor at W = 50 nm is plotted in Fig. 3.

Three models are generally used to describe the frequency dependence of silver: Drude, Drude-Debye (DD), and Lorentz-Drude (LD) [42–44]. Among these, the Drude model is the most classical method for obtaining the dielectric constant of the medium as it fits well with the experimental data at short wavelengths [45]. However, the Drude model generates significant errors in the long wavelengths. The DD model employs the dielectric constant as a frequency-dependent parameter. The calculation of the LD model is complex. Nonetheless, LD is the only model that considers the interband transitions and the obtained numerical results match closely with the experimental data [46,47]. Therefore, this article adopts the LD model to

Optics EXPRESS

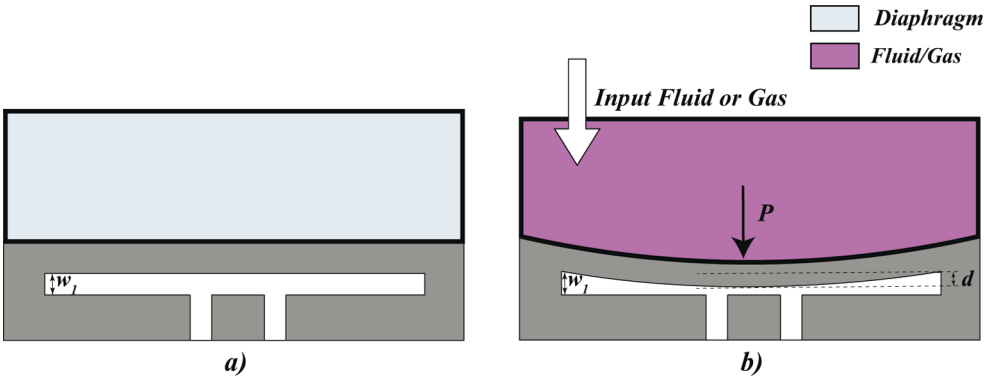

Fig. 2. a) Schematic of the resonator when no pressure is applied. b) Deformation of the resonator by d nm upon applied pressure, P Pa.

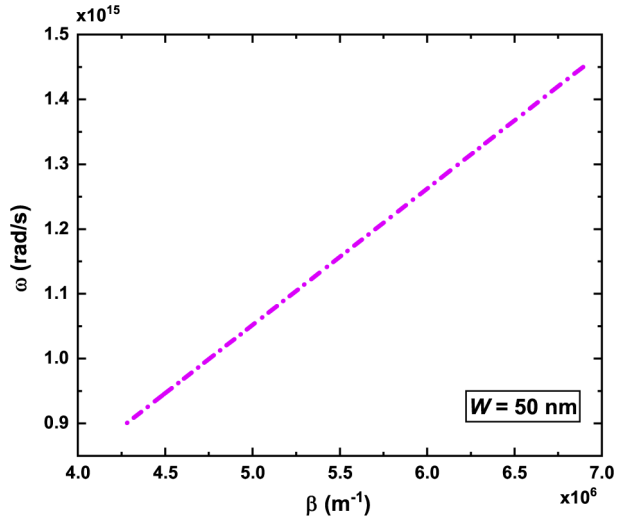

Fig. 3. Dispersion plot for the illustrated sensor at W = 50 nm.

express the frequency dependence of silver through the following equation [48],

$$\varepsilon_{silver}(\omega) = 1 - \frac{\omega_p^2}{\omega^2 - i\omega\Gamma_0} + \sum_{n=1}^{6} \frac{f_n\omega_n^2}{\omega_n^2 - \omega^2 + i\omega\Gamma_n}, \tag{4}$$

where, $\varepsilon_{silver}(\omega)$ represents the complex permittivity of silver. ω_p and ω_n are the plasma and resonant frequencies, respectively. In addition, f_n, Γ_n, and Γ_0 mean the oscillator strength, damping frequency, and collision frequency, respectively. Table 2 lists the numerical values of these parameters.

The numerical analysis of the modeled sensor is performed in the commercial EM simulator COMSOL Multiphysics 5.3, employing the Finite Element Method (FEM). The designed setup incorporates scattering boundary condition to absorb the outgoing EM waves and avoid reflections. Moreover, extra-fine triangular meshing is deployed around the waveguide and the resonator for the discretization of the structure (Fig. 4). Two ports labeled P_i and P_o are placed at the input and output sides, respectively to measure power flow and calculate transmittance as, $T = P_o/P_i$ [6].

Optics EXPRESS

Table 2. LD parameters for Ag [48].

Parameters	Values	Unit
Plasma frequency ($\hbar\omega_p$)	9.01	eV
Collision frequency (Γ_0)	0.048	eV
Oscillator strength (f_n)	[0.845; 0.065; 0.124; 0.011; 0.840; 5.646]	-
Damping frequency (Γ_n)	[0.048; 3.886; 0.452; 0.065; 0.916; 2.419]	eV
Resonant frequency (ω_n)	[0; 0.816; 4.481; 8.185; 9.083; 20.29]	eV

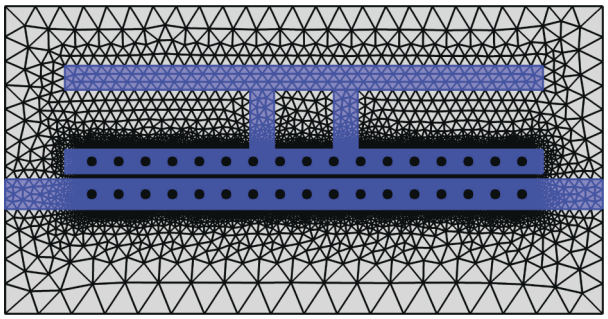

Fig. 4. Extra-fine triangular meshing of the proposed model.

The electron-beam lithography (EBL) can be used to fabricate the proposed nanosensor. EBL is equipped with sub-10 nm resolution and can write custom designs. On the silicon substrate, a thin coating of silver is deposited, followed by the desired pattern. Wet chemical etching, such as the use of water and dilute nitric acid, can be used to remove the surplus silver [49,50].

3. Numerical analysis and discussion

Figure 5 displays the transmittance spectrum when $d = 0$ nm (no pressure is applied). A resonant dip exists at the wavelength, $\lambda_{res} = 1482.47$ nm. To comprehend the resonance within the proposed structure, both magnetic field intensity, $|H| = (H_z^2)^{1/2}$ and electric field intensity, $|E| = (E^{x2}+E^{y2})^{1/2}$ are plotted in Fig. 6(a) and Fig. 6(b), respectively. It is observed that the dominant magnetic field exists within the upper horizontal slot where pressure is applied, whereas the dominant electric field exists around the NRs. Since most of the input energy is trapped within the resonator, the transmittance value reduces (Fig. 5).

Figure 2(b) illustrates the bending down of the top silver layer upon the application of pressure, P Pa. It is observed that the bent silver portion reduces the volume of the resonator. The deformed resonator causes a corresponding wavelength shift due to the coupling of the input light to the resonator on its way to the output port. Slater's law relates the deformation of the resonator and the wavelength shift through the following equation [51]:

$$\delta f/_f = -\left(\varepsilon_0 E^2 - \mu_0 H^2\right) \delta V \Big/ \int_V \left(\varepsilon_0 E^2 + \mu_0 H^2\right) \delta V, \tag{5}$$

where, f, E, H, and V refer to the resonant frequency, electric field intensity, magnetic field intensity, and volume of the resonating cavity, respectively and the values are listed in Table 3. Since the designed schematic is 2D, the height of the device is infinity. However, for practical fabrication, any height greater than 800 nm will result in close match with the simulations [37]. Hence, the height is taken as 900 nm in Table 3 to calculate the volume.

Optics EXPRESS

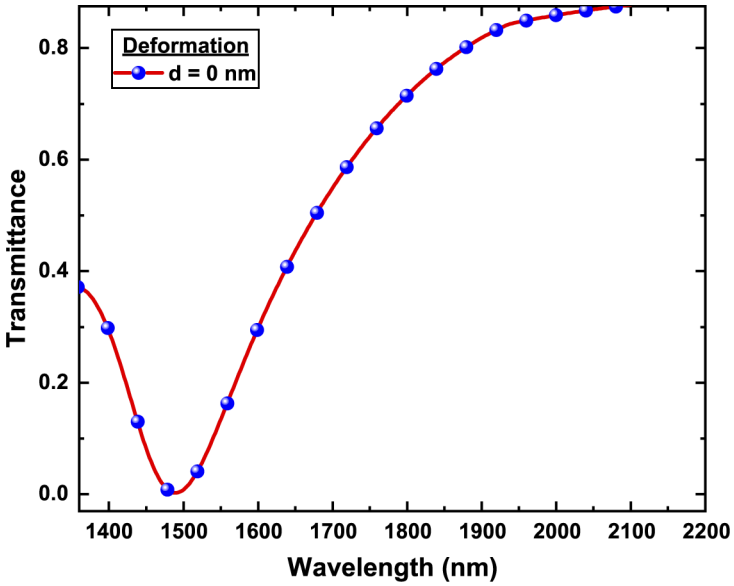

Fig. 5. Transmittance spectrum for $d = 0$ nm.

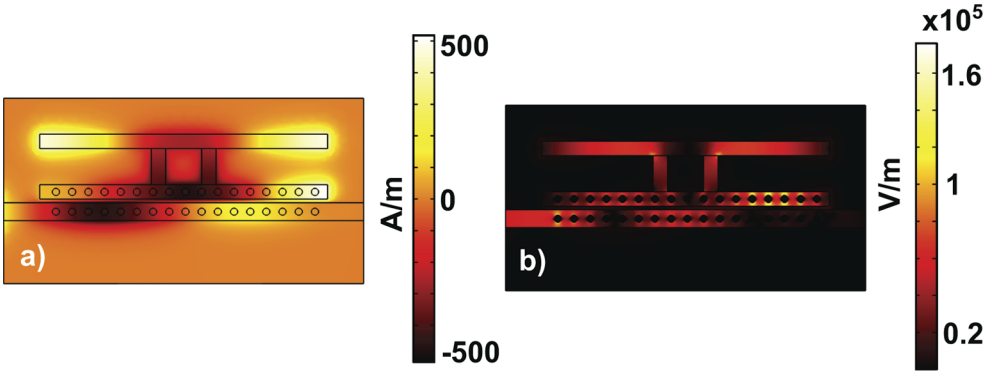

Fig. 6. a) $|H| = (H_z{}^2)^{1/2}$ and b) $|E| = (E^{x2}+E^{y2})^{1/2}$ profiles at $\lambda_{res} = 1482.47$ nm.

Table 3. Slater's law parameters at the resonant condition.

f (THz)	$\|H\|_{max}$ (A/m)	$\|E\|_{max}$ (V/m)	V (nm^3)
202.36	500 (Fig. 6(a))	1.65×10^5 (Fig. 6(b))	$800 \times 40 \times 900$

Optics EXPRESS

Equation (5) states that if the resonating cavity is dominated by the magnetic field and undergoes deformation, the resonant wavelength experiences a redshift. Otherwise, when the resonating cavity is dominated by the electric field and undergoes deformation, the resonant wavelength experiences a blueshift.

4. Pressure sensing

The deformation amount d is varied from 0 nm to 10 nm, with a step size of 2 nm to establish the relationship between the resonant wavelength and d. With increasing d, the resonant wavelength experiences a redshift (Fig. 7) due to the enhancement of cavity plasmon resonance (CPR). The absorption and strong coupling of light within the resonator cavity generate this CPR effect [52,53]. The redshift can also be explained using Eq. (5). The upper horizontal slot is dominated by the magnetic field (Fig. 6(a)). Hence, when d increases, the resonant wavelength moves toward longer wavelength region. Moreover, the resonant wavelength and d exhibit a linear relationship, as demonstrated in Fig. 8.

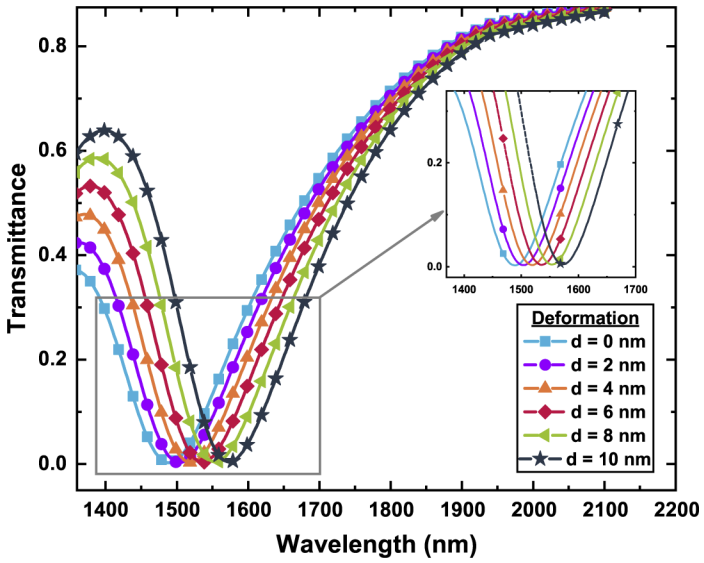

Fig. 7. Transmittance spectrum for d = 0 nm to d = 10 nm.

Assuming the upper silver layer as a plane plate with a thickness of h and a length of l, applied pressure P and deformation d can be related by the following equation [33],

$$P = {2Y_{Ag}h^3d}\Big/{l^4}, \tag{6}$$

where, Y_{ag} is Young's modulus of silver with a value of 7.5×10^{10} Pa. Furthermore, from Fig. 8, the resonant wavelength shift $\Delta\lambda_{res}$ and d is related with a constant of proportionality β and the resulting equation is as follows [33],

$$P = {2Y_{Ag}h^3\Delta\lambda_{res}}\Big/{\beta l^4}. \tag{7}$$

The performance of a pressure sensor is evaluated by the sensitivity value. Pressure sensitivity (S) can be expressed as [35],

$$S = {\Delta\lambda_{res}}/{\Delta P} = {l^4\Delta\lambda_{res}}\Big/{2Y_{Ag}h^3\Delta d}, \tag{8}$$

Optics EXPRESS

where, Δd is the corresponding difference between two deformation values. From Fig. 8, for Δd = 10 nm, the resonant wavelength shift is 92.93 nm. Hence, using Eq. (8), maximum sensitivity of 25.4 nm/MPa is obtained. Table 4 compares the suggested nanosensor with existing literature. It is observed that the proposed schematic displays the highest sensitivity reported to date (≈ 53.94% higher than [35]).

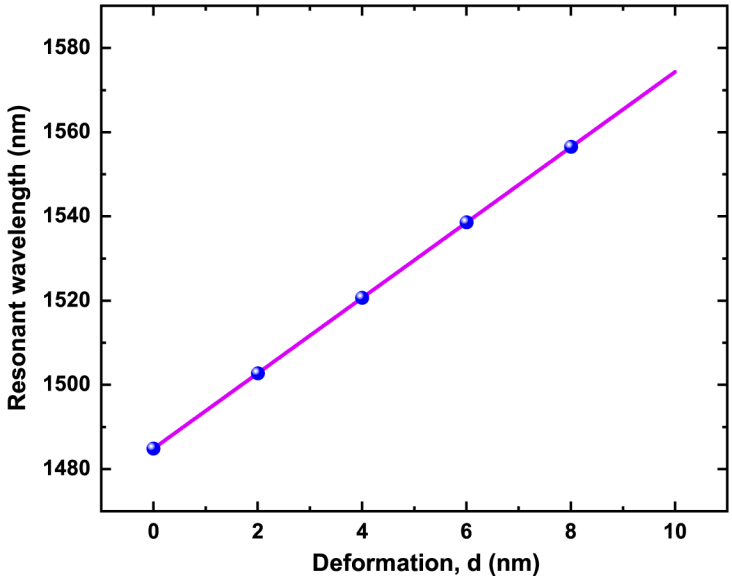

Fig. 8. Resonant wavelength vs. deformation graph.

Table 4. Comparison of pressure sensitivity with recent literature.

Reference	Sensitivity (nm/MPa)	Year
This work	25.4	2021
[35]	16.5	2018
[34]	8.5	2016
[4]	5	2020
[29]	4.29	2018
[28]	3.42	2008
[33]	2.12	2016
[27]	1.47	2012
[26]	1.198	2020
[25]	0.0117	2012
[24]	0.0116	2020

5. Influence of NRs on the proposed structure

Previously reported pressure sensors did not include any NRs. Thus, to further elucidate the effect of NRs on pressure sensitivity, numerous structures are simulated (Fig. 9(a) to Fig. 9(g)), and Table 5 summarizes the corresponding results. Figure 9(a) shows the transmittance profile for d = 0 nm and d = 10 nm when NRs are absent within the proposed schematic. Observing Table 5, the absence of NRs results in the lowest pressure sensitivity.

Optics EXPRESS

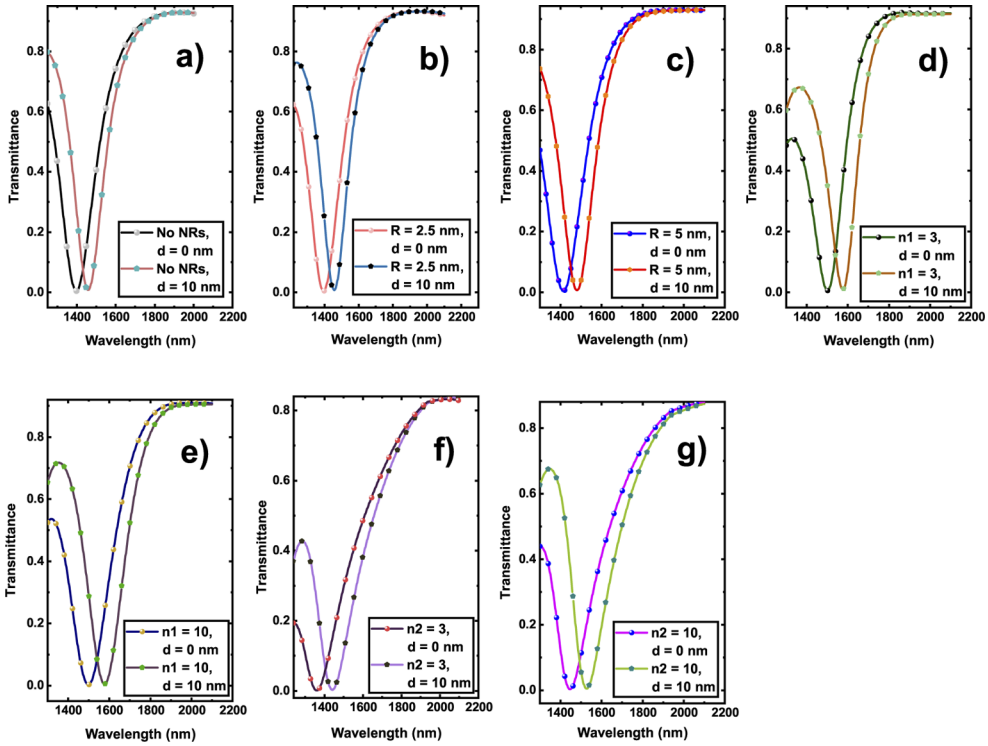

Fig. 9. Transmittance spectra for $d = 0$ nm and $d = 10$ nm when a) there are no NRs, b) $R = 2.5$ nm, c) $R = 5$ nm, d) $n_1 = 3$, e) $n_1 = 10$, f) $n_2 = 3$, and g) $n_2 = 10$.

Table 5. Influence of NRs on pressure sensitivity.

Case	Resonant wavelength shift (nm)	Pressure sensitivity (nm/MPa)
No NRs	57.71	15.76
$R = 2.5$ nm	59.43	16.23
$R = 5$ nm	67.52	18.44
$n_1 = 3$	74.28	20.29
$n_1 = 10$	80.3	21.93
$n_2 = 3$	77.77	21.24
$n_2 = 10$	80.98	22.12

Optics EXPRESS

Afterward, transmittance profiles for d = 0 nm and d = 10 nm are plotted for different NR parameters, for example, R (Fig. 9(b) and Fig. 9(c)), n_1 (Fig. 9(d) and Fig. 9(e)), and n_2 (Fig. 9(f) and Fig. 9(g)) while the remaining parameters stay constant. Table 5 indicates that increasing R, n_1, and n_2 generate longer resonant wavelength shifts, enhancing pressure sensitivity. The strong coupling of light within the gaps around NRs intensifies the energy of the resonating SPPs and hence causes redshift. This phenomenon is known as gap plasmon resonance (GPR) [54–58].

Considering all these aspects and after extensive simulations, the NR parameters of the illustrated sensor have been fixed as R = 10 nm, n_1 = 17, and n_2 = 17 to generate maximum pressure sensitivity of 25.4 nm/MPa.

6. Conclusion

In this article, a MIM optical pressure sensor decorated with silver NRs is proposed and numerically analyzed through the FEM. Transmittance spectra display a redshift for increasing pressure. Moreover, the resonant wavelength and deformation exhibit a linear association. The correlation between pressure and equivalent deformation is also explored, as well as a maximum pressure sensitivity of 25.4 nm/MPa is calculated. The article also discusses the influence of NRs on pressure sensitivity and summarizes the findings. Due to high sensitivity and compactness, the proposed sensor is a potential contender for different on-chip sensing tasks.

Acknowledgment. The authors would like to thank the Department of Electrical and Electronic Engineering of the Islamic University of Technology for their utmost support.

Disclosures. The authors declare no conflicts of interest.

Data availability. No data were generated or analyzed in the presented research.

References

1. W. L. Barnes, A. Dereux, and T. W. Ebbesen, "Surface plasmon subwavelength optics," Nature **424**(6950), 824–830 (2003).
2. Y.-F. Chau, Z.-H. Jiang, H.-Y. Li, G.-M. Lin, F.-L. Wu, and W.-H. Lin, "Localized resonance of composite core-shell nanospheres, nanobars and nanospherical chains," Prog. Electromagn. Res. **28**, 183–199 (2011).
3. Y.-F. Chau, "Surface plasmon effects excited by the dielectric hole in a silver-shell nanospherical pair," Plasmonics **4**(4), 253–259 (2009).
4. F. Moradiani, A. Farmani, M. H. Mozaffari, M. Seifouri, and K. Abedi, "Systematic engineering of a nanostructure plasmonic sensing platform for ultrasensitive biomaterial detection," Opt. Commun. **474**, 126178 (2020).
5. Y.-F. Chau, H.-H. Yeh, and D. P. Tsai, "Surface plasmon effects excitation from three-pair arrays of silver-shell nanocylinders," Phys. Plasmas **16**(2), 022303 (2009).
6. M. F. Hassan, R. H. Sagor, I. Tathfif, K. S. Rashid, and M. Radoan, "An optimized dielectric-metal-dielectric refractive index nanosensor," IEEE Sens. J. **21**(2), 1461–1469 (2021).
7. D. K. Gramotnev and S. I. Bozhevolnyi, "Plasmonics beyond the diffraction limit," Nat. Photonics **4**(2), 83–91 (2010).
8. G. V. Naik, V. M. Shalaev, and A. Boltasseva, "Alternative plasmonic materials: beyond gold and silver," Adv. Mater. **25**(24), 3264–3294 (2013).
9. M. W. Chen, Y.-F. Chau, and D. P. Tsai, "Three-dimensional analysis of scattering field interactions and surface plasmon resonance in coupled silver nanospheres," Plasmonics **3**(4), 157–164 (2008).
10. C.-T. C. Chao, Y.-F. C. Chau, and H.-P. Chiang, "Highly sensitive metal-insulator-metal plasmonic refractive index sensor with a centrally coupled nanoring containing defects," J. Phys. D: Appl. Phys. **54**(11), 115301 (2021).
11. Y.-F. C. Chau, "Mid-infrared sensing properties of a plasmonic metal–insulator–metal waveguide with a single stub including defects," J. Phys. D: Appl. Phys. **53**(11), 115401 (2020).
12. N. Amoosoltani, K. Mehrabi, A. Zarifkar, A. Farmani, and N. Yasrebi, "Double-ring resonator plasmonic refractive index sensor utilizing dual-band unidirectional reflectionless propagation effect," Plasmonics **16**(4), 1277–1285 (2021).
13. S. Zubaidah binti Haji Jumat, C.-T. Chou Chao, Y.-F. Chou Chau, A. H. Mahadi, M. R. R. Kooh, N. Kumara, and H.-P. Chiang, "Plasmonic refractive index sensor based on the combination of rectangular and circular resonators including baffles," Chin. J. Phys. **71**, 286–299 (2021).
14. M. R. Rakhshani, "Tunable and sensitive refractive index sensors by plasmonic absorbers with circular arrays of nanorods and nanotubes for detecting cancerous cells," Plasmonics **15**(6), 2071–2080 (2020).
15. M. R. Rakhshani, "Wide-angle perfect absorber using a 3d nanorod metasurface as a plasmonic sensor for detecting cancerous cells and its tuning with a graphene layer," Photonics and Nanostructures-Fundamentals Appl. **43**, 100883 (2021).

Optics EXPRESS

16. M. R. Rakhshani, "Three-dimensional polarization-insensitive perfect absorber using nanorods array for sensing and imaging," IEEE Sens. J. **20**(23), 14166–14172 (2020).
17. S. G. Shafagh, H. Kaatuzian, and M. Danaie, "Analysis, design and simulation of mim plasmonic filters with different geometries for technical parameters improvement," Commun. Theor. Phys. **72**(8), 085502 (2020).
18. L. S. Dizaj, K. Abbasian, and T. Nurmohammadi, "A three-core hybrid plasmonic polarization splitter designing based on the hybrid plasmonic waveguide for utilizing in optical integrated circuits," Plasmonics **15**(6), 2213–2221 (2020).
19. M. G. Saber, L. Xu, R. H. Sagor, Y. Wang, A. Kumar, D. Mao, E. El-Fiky, D. Patel, A. Samani, Z. Xing, M. Jacques, Y. D'Mello, and D. V. Plant, "Integrated polarisation handling devices," IET Optoelectron. **14**(3), 109–119 (2020).
20. G. Z. Mashanovich, "Optical switches and modulators in deep freeze," Nat. Mater. **19**(11), 1135–1136 (2020).
21. S. Upadhyay, V. L. Kalyani, and C. Charan, "Designing and optimization of nano-ring resonator-based photonic pressure sensor," in *Proceedings of International Conference on ICT for Sustainable Development*, (Springer, 2016), pp. 269–278.
22. D. Donlagic and E. Cibula, "All-fiber high-sensitivity pressure sensor with sio 2 diaphragm," Opt. Lett. **30**(16), 2071–2073 (2005).
23. J. H. Osório, J. G. Hayashi, Y. A. Espinel, M. A. Franco, M. V. Andrés, and C. M. Cordeiro, "Photonic-crystal fiber-based pressure sensor for dual environment monitoring," Appl. Opt. **53**(17), 3668–3672 (2014).
24. V. S. Chaudhary, D. Kumar, R. Mishra, and S. Sharma, "Hybrid dual core photonic crystal fiber as hydrostatic pressure sensor," Optik **210**, 164497 (2020).
25. S. Olyaee and A. A. Dehghani, "Nano-pressure sensor using high quality photonic crystal cavity resonator," in *2012 8th International Symposium on Communication Systems, Networks & Digital Signal Processing (CSNDSP)*, (IEEE, 2012), pp. 1–4.
26. Z. Hong-kun, Z. Yong, Z. Qiang, and L. Ri-qing, "High sensitivity optical fiber pressure sensor based on thin-walled oval cylinder," Sens. Actuators, A **310**, 112042 (2020).
27. X. Zhao, J. Tsai, H. Cai, X. Ji, J. Zhou, M. Bao, Y. Huang, D. Kwong, and A. Q. Liu, "A nano-opto-mechanical pressure sensor via ring resonator," Opt. Express **20**(8), 8535–8542 (2012).
28. H. Fu, H. Y. Tam, L.-Y. Shao, X. Dong, P. K. A. Wai, C. Lu, and S. K. Khijwania, "Pressure sensor realized with polarization-maintaining photonic crystal fiber-based sagnac interferometer," Appl. Opt. **47**(15), 2835–2839 (2008).
29. M. Yao, X. Ouyang, J. Wu, A. P. Zhang, H.-Y. Tam, and P.-K. A. Wai, "Optical fiber-tip sensors based on in-situ μ-printed polymer suspended-microbeams," Sensors **18**(6), 1825 (2018).
30. Y. Fang and M. Sun, "Nanoplasmonic waveguides: towards applications in integrated nanophotonic circuits," Light: Sci. Appl. **4**(6), e294 (2015).
31. J. Zhu and G. Wang, "Sense high refractive index sensitivity with bragg grating and mim nanocavity," Results Phys. **15**, 102763 (2019).
32. M. R. Rakhshani, "Optical refractive index sensor with two plasmonic double-square resonators for simultaneous sensing of human blood groups," Photonics and Nanostructures-Fundamentals Appl. **39**, 100768 (2020).
33. J. Wu, P. Lang, X. Chen, and R. Zhang, "A novel optical pressure sensor based on surface plasmon polariton resonator," J. Mod. Opt. **63**(3), 219–223 (2016).
34. G. Duan, P. Lang, L. Wang, L. Yu, and J. Xiao, "An optical pressure sensor based on π-shaped surface plasmon polariton resonator," Mod. Phys. Lett. B **30**(21), 1650284 (2016).
35. P. Palizvan, S. Olyaee, and M. Seifouri, "An optical mim pressure sensor based on a double square ring resonator," Photonic Sens. **8**(3), 242–247 (2018).
36. C. S. Sander, J. W. Knutti, and J. D. Meindl, "A monolithic capacitive pressure sensor with pulse-period output," IEEE Trans. Electron Devices **27**(5), 927–930 (1980).
37. R. Al Mahmud, M. O. Faruque, and R. H. Sagor, "A highly sensitive plasmonic refractive index sensor based on triangular resonator," Opt. Commun. **483**, 126634 (2021).
38. M. F. Hassan, R. H. Sagor, M. R. Amin, M. R. Islam, and M. S. Alam, "Point of care detection of blood electrolytes and glucose utilizing nano-dot enhanced plasmonic biosensor," IEEE Sens. J. **21**(16), 17749–17757 (2021).
39. M. Mansouri, A. Mir, A. Farmani, and M. Izadi, "Numerical modeling of an integrable and tunable plasmonic pressure sensor with nanostructure grating," Plasmonics **16**(1), 27–36 (2021).
40. M. F. Hassan, I. Tathfif, M. Radoan, and R. H. Sagor, "A concentric double-ring resonator based plasmonic refractive index sensor with glucose sensing capability," in *2020 IEEE REGION 10 CONFERENCE (TENCON)*, (IEEE, 2020), pp. 91–96.
41. R. H. Sagor, M. F. Hassan, A. A. Yaseer, E. Surid, and M. I. Ahmed, "Highly sensitive refractive index sensor optimized for blood group sensing utilizing the fano resonance," Appl. Nanosci. **11**(2), 521–534 (2021).
42. Y.-F. Chou Chau, C.-T. Chou Chao, H. J. Huang, M. R. R. Kooh, N. T. R. N. Kumara, C. M. Lim, and H.-P. Chiang, "Ultrawide bandgap and high sensitivity of a plasmonic metal-insulator-metal waveguide filter with cavity and baffles," Nanomaterials **10**(10), 2030 (2020).
43. Y. Z. Ho, W. T. Chen, Y.-W. Huang, P. C. Wu, M. L. Tseng, Y. T. Wang, Y.-F. Chau, and D. P. Tsai, "Tunable plasmonic resonance arising from broken-symmetric silver nanobeads with dielectric cores," J. Opt. **14**(11), 114010 (2012).
44. H. Shi, S. Yan, X. Yang, H. Su, X. Wu, and E. Hua, "Nanosensor based on fano resonance in a metal-insulator-metal waveguide structure coupled with a half-ring," Results Phys. **21**, 103842 (2021).

Optics EXPRESS

45. P. B. Johnson and R. W. Christy, "Optical Constant of the Nobel Metals," Phys. Rev. B **6**(12), 4370–4379 (1972).
46. S. A. Maier, *Plasmonics: fundamentals and applications* (Springer Science & Business Media, 2007).
47. K. S. Rashid, M. F. Hassan, A. A. Yaseer, I. Tathfif, and R. H. Sagor, "Gas-sensing and label-free detection of biomaterials employing multiple rings structured plasmonic nanosensor," Sens. Bio-Sensing Res. **33**, 100440 (2021).
48. A. D. Rakić, A. B. Djurišić, J. M. Elazar, and M. L. Majewski, "Optical properties of metallic films for vertical-cavity optoelectronic devices," Appl. Opt. **37**(22), 5271–5283 (1998).
49. M. A. A. Butt and N. Kazanskiy, "Enhancing the sensitivity of a standard plasmonic mim square ring resonator by incorporating the nano-dots in the cavity," Photonics Lett. Pol. **12**(1), 1–3 (2020).
50. M. Butt, S. Khonina, and N. Kazanskiy, "An array of nano-dots loaded mim square ring resonator with enhanced sensitivity at nir wavelength range," Optik **202**, 163655 (2020).
51. H. Wang, J. Yang, J. Zhang, J. Huang, W. Wu, D. Chen, and G. Xiao, "Tunable band-stop plasmonic waveguide filter with symmetrical multiple-teeth-shaped structure," Opt. Lett. **41**(6), 1233–1236 (2016).
52. Y.-F. C. Chau, J.-C. Jiang, C.-T. C. Chao, H.-P. Chiang, and C. M. Lim, "Manipulating near field enhancement and optical spectrum in a pair-array of the cavity resonance based plasmonic nanoantennas," J. Phys. D: Appl. Phys. **49**(47), 475102 (2016).
53. Y.-F. C. Chau, C.-T. C. Chao, J.-Y. Rao, H.-P. Chiang, C. M. Lim, R. C. Lim, and N. Y. Voo, "Tunable optical performances on a periodic array of plasmonic bowtie nanoantennas with hollow cavities," Nanoscale Res. Lett. **11**(1), 411 (2016).
54. Y.-F. C. Chau, C.-T. C. Chao, and H.-P. Chiang, "Ultra-broad bandgap metal-insulator-metal waveguide filter with symmetrical stubs and defects," Results Phys. **17**, 103116 (2020).
55. Y.-F. Chou Chau, C.-T. Chou Chao, H. J. Huang, M. R. R. Kooh, N. Kumara, C. M. Lim, and H.-P. Chiang, "Perfect dual-band absorber based on plasmonic effect with the cross-hair/nanorod combination," Nanomaterials **10**(3), 493 (2020).
56. Y.-F. Chou Chau, C.-T. Chou Chao, H. J. Huang, N. Kumara, C. M. Lim, and H.-P. Chiang, "Ultra-high refractive index sensing structure based on a metal-insulator-metal waveguide-coupled t-shape cavity with metal nanorod defects," Nanomaterials **9**(10), 1433 (2019).
57. M. Butt, N. Kazanskiy, and S. Khonina, "Nanodots decorated asymmetric metal–insulator–metal waveguide resonator structure based on fano resonances for refractive index sensing application," Laser Phys. **30**(7), 076204 (2020).
58. C.-T. Chou Chao, Y.-F. Chou Chau, H. J. Huang, N. Kumara, M. R. R. Kooh, C. M. Lim, and H.-P. Chiang, "Highly sensitive and tunable plasmonic sensor based on a nanoring resonator with silver nanorods," Nanomaterials **10**(7), 1399 (2020).